Int J CARS (2016) 11:1965–1977
DOI 10.1007/s11548-016-1443-y

ORIGINAL ARTICLE

A computer-aided tracking and motion analysis with ultrasound (CAT & MAUS) system for the description of hip joint kinematics

Rui Jia[1] · **Stephen Mellon**[2] · **Paul Monk**[2] · **David Murray**[2] · **J. Alison Noble**[1]

Received: 19 January 2016 / Accepted: 6 June 2016 / Published online: 16 June 2016

Abstract
Purpose Investigation of joint kinematics contributes to developing a better understanding of musculoskeletal conditions. However, the most commonly used optoelectronic motion analysis systems cannot determine the movements of underlying bone landmarks with high accuracy because of soft tissue artefacts. The aim of this paper was to present a computer-aided measurement system to track the underlying bone anatomy in a 3D global coordinate frame and describe hip joint kinematics of ten healthy volunteers during gait.
Methods We have developed a measurement tool with an image-based computer-aided post-processing pipeline for automatic bone segmentation in ultrasound (US) images and a globally optimal 3D surface-to-surface registration method to quantify hip joint movements. The segmentation algorithm exploits US intensity profiles, including information about the integrated backscattering, acoustic shadows, and local phase features. A global optimization method is applied based on the traditional iterative closest point registration algorithm, which is robust to initialization. The International Society of Biomechanics recommended joint kinematics descriptor has been adapted to calculate the joint kinematics.
Results The developed system prototype has been validated with a ball-joint femoral phantom and tested in vivo with 10 volunteers. The maximum Euclidean distance error of the automatic bone segmentation is less than 2 pixels (approximately 0.2 mm). The maximum absolute rotation angle error is less than 4°.
Conclusion This computer-aided tracking and motion analysis with ultrasound (CAT & MAUS) system shows the feasibility of describing hip joint kinematics for clinical investigation and diagnosis using an image-based solution.

Keywords Bone ultrasound · Segmentation · Registration · Joint kinematics

Introduction

It is estimated that nearly one-quarter of adults in England are affected by musculoskeletal problems that limit everyday activities [1]. This rate may be even higher in developing countries because of limited access to clinical treatment. It is thought that joint kinematics play a role in the development of a number of pathologies [2]. However, state-of-the-art diagnosing modalities have various limitations for describing joint kinematics, which include exposure to radiation with CT and fluoroscopy and space limitation for MRI [3].

Currently, joint kinematics analysis primarily makes use of motion analysis (MA) systems to determine the movement of the skeleton. Optoelectronic MA systems are essentially a group of infrared cameras that capture the 3D positions of skin-attached retro-reflective markers placed on bony landmarks on a test subject. Although the objective is to capture the position of the rigid skeleton, the markers are attached to the skin and are separated from bone by soft tissues. Thus, the markers shift, while the test subject is moving. This soft tissue artefact (STA) can cause an error of up to 30 mm for markers on the thigh during movements [4]. Evidence suggests that there is a significant discrepancy between the data obtained by this method and the true movement of the bone [3]. In order

✉ Rui Jia
rui.jia@eng.ox.ac.uk

[1] Institute of Biomedical Engineering, Department of Engineering Science, University of Oxford, Oxford, UK

[2] Nuffield Department of Orthopaedics, Rheumatology and Musculoskeletal Sciences, University of Oxford, Oxford, UK

to reveal the movement of the real underlying bony landmarks, ultrasound (US) has previously been combined with a MA system to directly monitor under-skin bone structures [3]. However, the accuracy of this technique has been found to be highly dependent upon the sonographer's experience and knowledge of anatomy as an identical bony landmark has to be aligned each time to a manually drawn cross on the US screen. Moreover, for one subject examination, it can take 30–40 min to test four different poses of normal activity, which reduces the repeatability of the examination and means the method is not well-suited as it stands for clinical translation. Thus, in order to achieve a more automatic and accurate joint kinematics description, we introduce a computer-aided post-processing pipeline including an automatic segmentation algorithm and a global 3D surface registration method to the current motion analysis and ultrasound (MAUS) system.

Bone structure detection in US images is a precursor to further analysis, such as structure tracking, 3D surface reconstruction, or registration. Due to speckle and variable bone response under US, automatically identifying the bone surface in US data is non-trivial. An automatic bone segmentation algorithm based on a bone probability map was performed giving a 0.3 mm accuracy in [5]. However, that algorithm was sensitive to areas like the fascia, which can be misdetected as bone. Local phase features were considered for bone segmentation in [6,7]. However, it was found to be non-trivial to reduce unwanted ridge-like responses due to soft tissues [8].

In order to locate the target bone structure, a three-dimensional (3D) surface-to-surface registration follows bone structure detection [9]. As the bone structure is a rigid body, in our work, we make use of rigid body registration, specifically the iterative closest point (ICP) algorithm, which is a commonly used method for finding the transformation between two 3D point clouds [10]. However, the traditional ICP method can get trapped in local minima of its cost function leading to an incorrect registration [11]. Yang et al. presented a globally optimal ICP framework that can register two point clouds correctly without a good initialization [12] and is suitable for position-fixed human medical imaging data.

Computer-aided post-processing algorithms have been developed to assist freehand US for computer-aided orthopaedic surgery [13]. Wein et al. presented automatic bone detection followed by US-to-CT registration to assist intra-operative planning [8]. However, the bores of CT scanners are commonly limited to around 600 mm which is too small for a subject to present a full range of motion, like gait. Moreover, exposure to radiation increases the risk of cancer. There has been very little attention given to US-to-US surface registration to quantify joint movements. Thus, in this paper, we suggest a US-to-US surface registration framework as part of a joint kinematics measurement system.

In this paper, we present a computer-aided tracking and motion analysis with ultrasound (CAT & MAUS) system for describing hip joint kinematics. In particular, we present a motion analysis with ultrasound (MAUS) system with an automatic bone segmentation algorithm based on a bone probability map, a globally optimal ICP surface registration method and the International Society of Biomechanics (ISB) recommended hip joint kinematics descriptor in "Methods" section. In vitro and in vivo tests are described in "Experiments" section and results are reported in "Results" section. A discussion of CAT & MAUS is presented in "Discussion" section. The paper concludes in "Conclusion" section.

Methods

This section introduces the CAT & MAUS system for describing hip joint kinematics. The schematic of the system is shown in Fig. 1. The full system consists of a the motion analysis with ultrasound system and computer post-processing.

Motion analysis with ultrasound system

A motion analysis with ultrasound (MAUS) system combines US with a motion analysis (MA) system to transform two-dimensional (2D) US images into 3D space based on the trajectory of the US probe captured by MA (leftmost part in Fig. 1). Retro-reflective markers are attached to the US probe to track its position in 3D. US images are transformed into 3D space using Euclidean transformation matrices [14,15].

An US scan of a target bony structure (the greater trochanter (GT) in our study) is constrained in a parallel sweep similar to [15], i.e. the US probe is moved such that consecutive US images are parallel (Fig. 2).

Automatic bone segmentation

The new bone segmentation algorithm can be summarized in two steps: bone probability mapping and dynamic programming optimization. We compare with the method of [5] in "Results" section.

Bone probability mapping

Firstly, we normalize the pixel intensities into the range 0–1 and smooth the US images with a Gaussian kernel with a standard deviation dependent upon the thickness of the bone surface under US (6 pixels in our case) to reduce speckle (Fig. 3a). Based on knowledge of scanning geometry and typical image appearance, the top 50 rows of an US image and pixels with normalized intensity lower than 0.125 are ignored as they are unlikely to be the bony anatomy. A binary mask

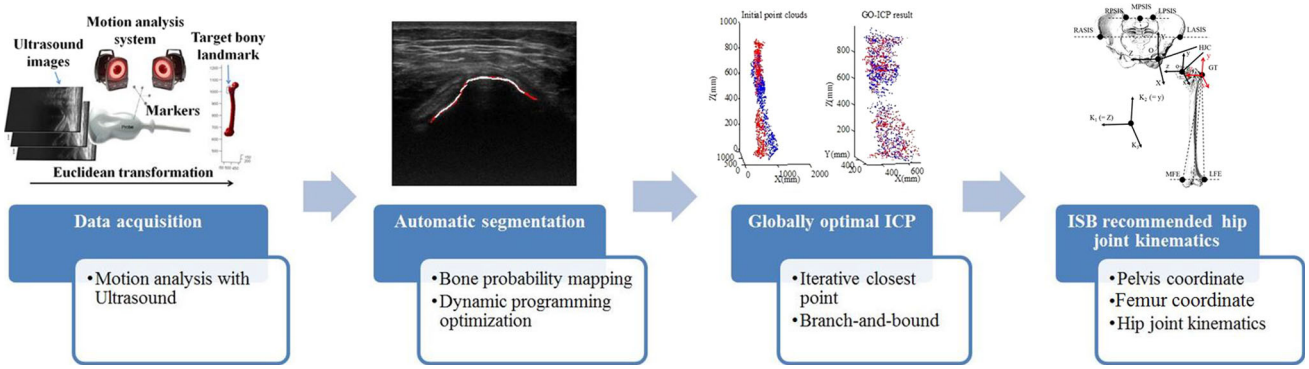

Fig. 1 Schematic of the proposed computer-aided tracking and motion analysis with ultrasound (CAT & MAUS) system

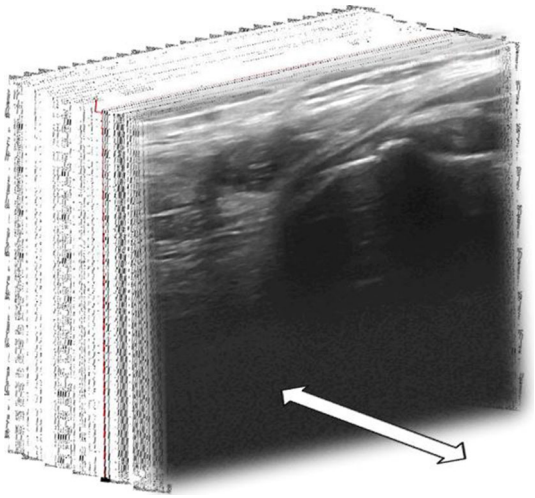

Fig. 2 Parallel US scanning

is employed to remove those pixels to increase processing speed (Fig. 3b).

The bone surface generates a strong reflection with a certain thickness. This response is higher in intensity than that from the soft tissue above the bone and the intensity of the area below the bone structure. Therefore, pixels with high intensity are more likely to be the bony structure. The Laplacian of Gaussian (LOG) filter is used to detect the reflection. In the area immediately above a bone structure in an US image, the LOG filter gives a positive response to the dark area on both sides of the bone, a negative response to the bright area of the bone and a zero response at the boundary. As we are only interested in negative values, we keep the negative values and zero the rest (Fig. 3c).

Due to its high acoustic impedance, most of the US energy is reflected at the bone surface. Thus, the region below the structure appears to be dark in US images. A shadow value for pixel *(a, b)* is calculated as a Gaussian weighted accumulation of the pixels below as in [5]. A typical shadow map is shown in Fig. 3d.

The bone structure appears as an intensity ridge in an US image and as such is a symmetric feature. Feature symmetry, extracted via local phase, estimated via the monogenic signal [16] is applied to enhance the probability of bone detection [7]. In this paper, we focus on log-gabor filters as used in previous work on US segmentation [17]. The ridge-like pattern in an US image presents a high value in the local amplitude, which is the square root value of the local energy, shown in Fig. 3e and a value of π in the local phase shown in Fig. 3f. Bone structures in an US image have a high value in the feature symmetry image. We detect the bone structure using multi-scale bandpass filtering, i.e. different wavelengths, and sum the results of feature symmetry images [17,18]. The wavelength set we used was 5, 10 and 15 pixels based on the thickness of the bone structure in US images [19]. This is shown in Fig. 3g.

In order to reduce the interference from the soft tissues above the bone structure, the integrated backscattering (IBS) energy along US scan lines are considered to enhance the probability of detection of the bone area as most of the US energy is backscattered at the bone surface. The IBS energy is the sum of all squared intensities above a given pixel on a scan line. The IBS energy of pixel (a, b), $IBS\,(a, b)$, is defined as:

$$IBS(a, b) = \sum_{i=1}^{a} I^2(i, b) \tag{1}$$

where $I(,)$ is the pixel intensity and i is the ith row of the US image. As a bone structure boundary should have higher acoustic impedance difference compared to the soft tissues above it, most of the US energy is reflected at the bone surface. Thus, the IBS energy of bone structures and the areas below is higher than for soft tissues above the bone (Fig. 3h).

The final bone probability map (Fig. 3i) is the normalized product of the Laplacian of Gaussian of the US image, the mask, the shadow map, the IBS energy, the local amplitude, the local phase and the feature symmetry. A threshold of the

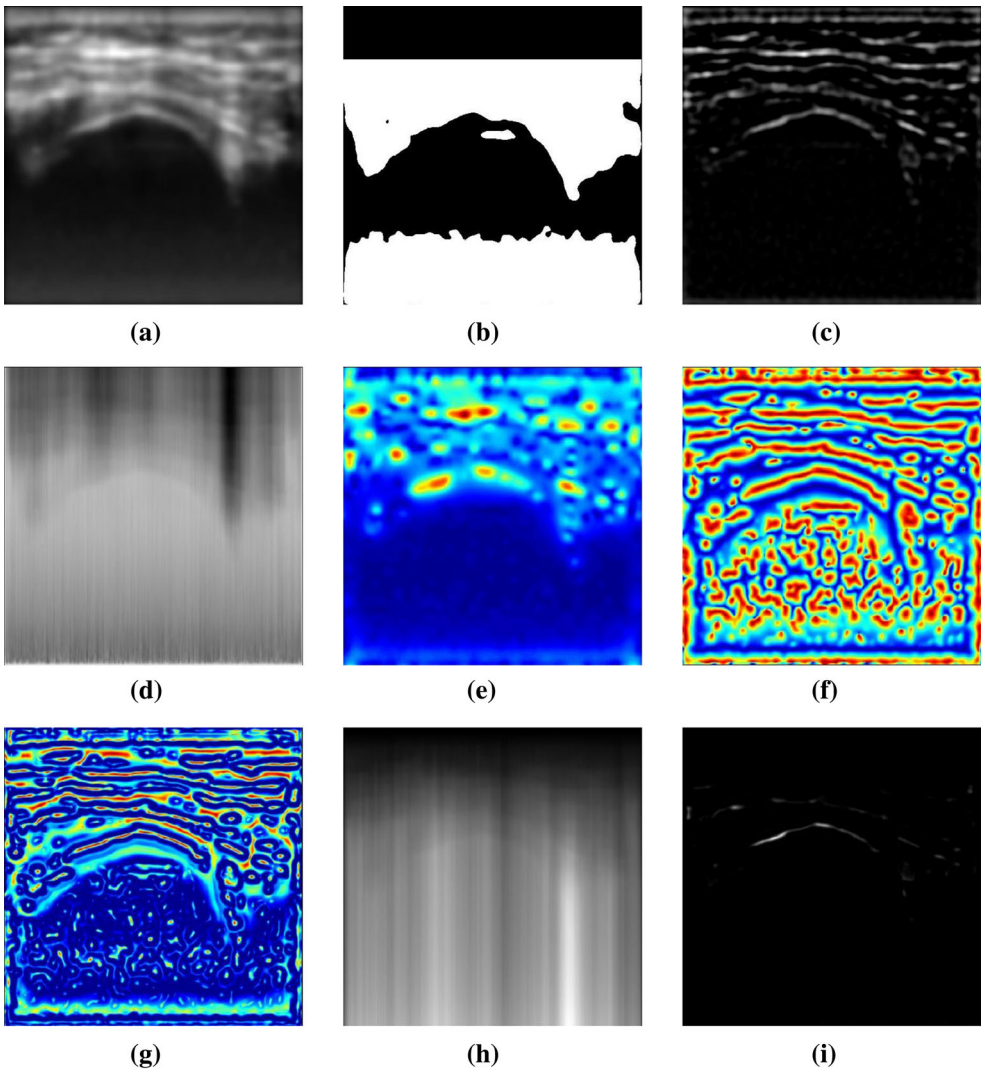

Fig. 3 **a** Image smoothed with Gaussian filter, **b** binary mask, **c** result after Laplacian of Gaussian filter, **d** shadow model, **e** local amplitude, **f** local phase, **g** feature symmetry, **h** integrated backscattering and **i** bone probability mapping

bone probability (the optimal value in our study is 0.15) is used to reduce responses attributed to noise.

Dynamic programming optimization

We follow a similar method to [5]. To segment the bone surface, it is assumed that there is only one pixel representing the bone for each column (vertical scan line) of the US image. Each pixel in each column belongs to one of the following three regions which are *bone*, *boneless* and *the jump* as illustrated in Fig. 4.

The existence of the bone structure in column s, *Seg(s)*, and its location is determined by minimizing a cost function which is composed of an internal and an external energy denoted as E_{int} and E_{ext}, respectively. The external energy is one minus the bone probability. The internal energy is defined for the three parts of the segmentation as in [5]:

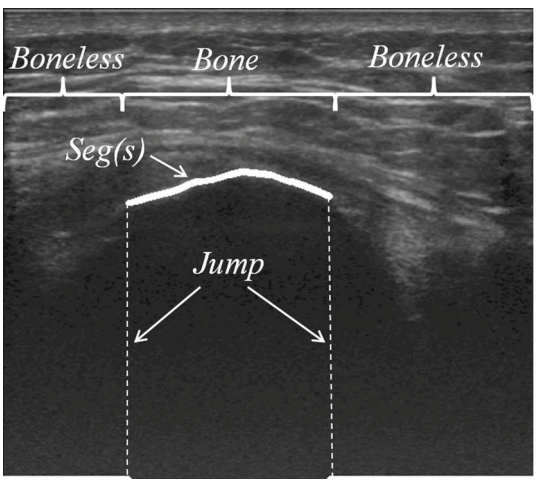

Fig. 4 Three parts of the bone segmentation Seg(s). *Note* the *white line* is thickened for better visualization

$$E_{\text{int}} = \begin{cases} \alpha \left\| \frac{\text{dSeg}}{\text{d}s} \right\|^2 + \beta \left\| \frac{\text{d}^2\text{Seg}}{\text{d}s^2} \right\|^2 + \gamma, & \text{Bone region} \\ \text{JumpCost}, & \text{Jump region} \\ \alpha {D_1}^2 + \beta {D_2}^2, & \text{Boneless region} \end{cases} \quad (2)$$

where α,β are the weights of the smoothness (the first derivative of Seg) and the curvature (the second derivative of Seg), γ is a small negative scalar to tune the connectivity. s is the index of the current pixel. A JumpCost penalizes the big jump between the *bone region* and *boneless region*. We set the smoothness and curvature to a constant value D_1 and D_2, respectively in the *boneless region* because there is no bone detection in the *boneless region*.

The cost of the segmentation is minimized by solving the recursive Eq. (3), and the index of the pixel (k, j) with its minima stored as in Eq. (4).

$$\text{Segmin}(i, j) = E_{\text{ext}}(i, j) + \min_k \{\text{Segmin}(k, j-1) + E_{\text{int}}(k, j)\} \quad (3)$$

$$\text{Idxmin}(i, j) = \underset{k}{\text{argmin}} \{\text{Segmin}(k, j-1) + E_{\text{int}}(k, j)\} \quad (4)$$

where $\text{Segmin}(i, j)$ and $\text{Idxmin}(i, j)$ are the minimum cost and its index of the segmentation from the first column to the pixel in the ith row and jth column. k is the row index.

Lastly, the optimal path is obtained by tracing back from the last column of the US image as Eq. (5):

$$\text{Seg}_{\text{opt}}(s) = \begin{cases} \text{LR} + 1, & s = \text{LC} \\ \text{Idxmin}[s+1, \text{Seg}_{\text{opt}}(s+1)], & s = 1, \ldots, (\text{LC} - 1) \end{cases} \quad (5)$$

where Seg_{opt} is the optimal segmentation path with minimum energy cost. LR and LC indicate the number of rows and columns of the US image which also represent the last row and last column, respectively.

Globally optimal 3D surface registration

Via the tracked position of the US probe, a 3D surface of the greater trochanter (GT) can be reconstructed from the automatic segmented bone structure [15,20]. During US scanning, the subject may move; therefore, before reconstructing the 3D bone surface, we correct all of the motion analysis frames based on the marker position in the first frame. Since the target bone structure is rigid, a rigid body registration algorithm can help to find the spatial transformation, i.e. rotations and translations between any two positions of the bone structure in 3D space. The 3D surface of the GT reconstructed using the US data collected at the standing position is defined as the reference (i.e. "model") instead of a pre-scanned CT volume [8], while surfaces reconstructed at other positions are defined as the "data".

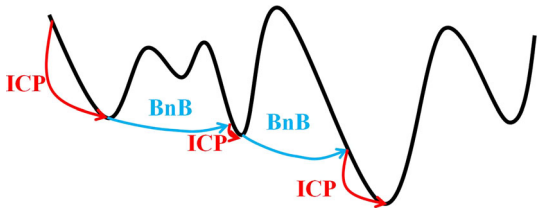

Fig. 5 Branch-and-bound global searched iterative closest point registration

Iterative closest point (ICP) registration registers data to model by minimizing the L_2-norm between those two surfaces. However, it fails at some positions when it is not well-initialized because of the local minimum trap. Yang et al. introduced a globally optimal search method using branch-and-bound (BnB) to overcome the drawback of the traditional ICP registration [12]. The method can be summarized as three steps. Firstly, use BnB to search the 3D Euclidean group which is a three dimensional combined space of the rotation and the translation. In order to search the optimal solution efficiently, the branch whose lower bound is higher than the other branch's upper bound is cut as it is computationally meaningless. Detailed definition of the upper and lower bounds in the BnB search were presented in [12]. Then, whenever a minimum cost solution is found, the ICP algorithm is called with an initialization starting at this solution to reduce the cost error. Finally, the upper bound of BnB search is updated by the ICP's result until convergence. The global BnB search is shown in Fig. 5.

We implemented this globally optimal ICP (GO-ICP) registration algorithm for our application. Using the results from GO-ICP, the joint rotation can then be quantified using the joint kinematics descriptor suggested by International Society of Biomechanics (ISB) as described in "Hip joint kinematics description" section.

Hip joint kinematics description

The International Society of Biomechanics (ISB) has suggested a definition of a local joint coordinate system for hip joint kinematics calculation [21]. We follow the ISB protocol with a minor adaption of the femoral coordinate system to define the hip joint kinematics.

Anatomical bony landmarks used

The bony landmarks of the pelvis and the thigh listed in Table 1 were used to define joint kinematics description. The methods to collect the data from these landmarks, either MA

Table 1 Bony landmarks of the pelvis and the thigh

Marker	Description	Methods
LASIS	Left anterior superior iliac spine	MA
RASIS	Right anterior superior iliac spine	MA
LPSIS	Left posterior superior iliac spine	MA
MPSIS	Mid posterior superior iliac spine	MA
RPSIS	Right posterior superior iliac spine	MA
GT	Greater trochanter	CAT & MAUS
LFE	Lateral femoral epicondyle	MA
MFE	Medial femoral epicondyle	MA

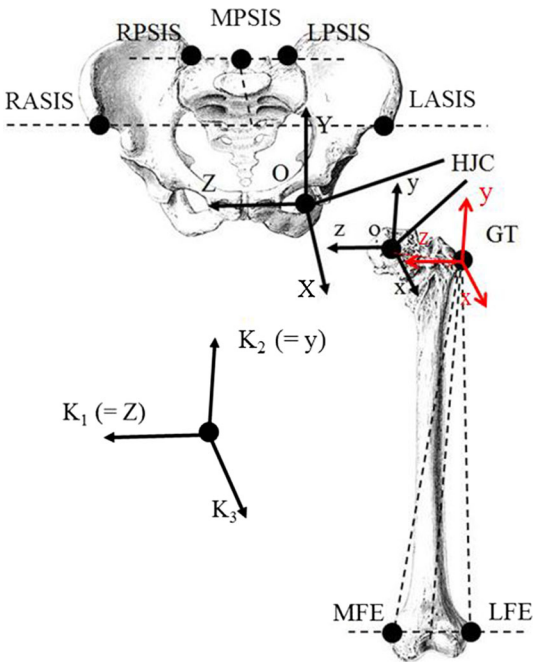

Fig. 6 *Left hip* joint coordinate systems, pelvic coordinate system (*XYZ*) adapted femoral coordinate system (*red xyz*) and the kinematics description

or CAT & MAUS are also shown in Table 1. Refer to Fig. 6 for a visual representation of the key terms.

Local bone structure coordinate systems

There are two coordinate systems that need to be related: the Pelvic coordinate system (PCS) and the Femoral coordinate system (FCS).

Pelvic coordinate system (PCS): (*X,Y,Z*)

The left hip joint centre (HJC) is defined as the origin of the Pelvic coordinate system (PCS). The HJC is estimated by the Nexus motion analysis software based on markers attached on the pelvis and the femur. The *Z* axis is parallel to the line pointing from the left anterior superior iliac spine (LASIS) to the right anterior superior iliac spine (RASIS) (Fig. 6). The *X* axis of the PCS is parallel to the line lying in the plane defined by the LASIS, the RASIS and the mid posterior superior iliac spine (MPSIS), pointing anteriorly from MPSIS and orthogonal to the *Z* axis. The *Y* axis of the PCS is perpendicular to both the *X* axis and the *Z* axis, pointing superiorly.

Femoral coordinate system (FCS): (x,y,z)

The origin of the Femoral coordinate system (FCS) is coincident with the origin of the PCS which is the HJC. ISB recommends that the *y* axis of the FCS is defined as the line joining the midpoint between the lateral femoral epicondyle (LFE) and the medial femoral epicondyle (MFE) and the HJC, pointing superiorly [21]. As the HJC in our study is an estimated landmark based on the physical parameters of the subject, it varies between different individuals. The uncertainty of the estimated HJC introduces errors. Thus, we redefine the *y* axis as parallel to the line pointing from the midpoint between the LFE and the MFE to the GT, pointing superiorly. The *z* axis of the FCS is orthogonal to the *y* axis and parallel to the line pointing from the LFE to the MFE. The *x* axis of the FCS is perpendcular to both the *y* axis and the *z* axis pointing anteriorly.

Hip joint kinematics description

After registering the GT from one pose to another pose, we quantify the hip joint kinematics using the registered underlying GT position in combination with the skin markers. As the hip joint is a ball joint, it rotates with 3 degrees of freedom during activity. Thus, the hip joint kinematics can be described as hip joint rotations in the sagittal plane, the transverse plan and the coronal plane around K_1, K_2 and K_3 axes, respectively. These joint rotations are described in the coordinate system (K_1, K_2, K_3) below.

Flexion/extension

The K_1 axis is an axis parallel to the *Z* axis of the pelvic coordinate system. We quantify the rotation angle around K_1 axis as flexion/extension which is the rotation in the sagittal plane.

Internal/external rotation

The K_2 axis is an axis parallel to the *y* axis of the femoral coordinate system. We quantify the rotation angle around K_2 axis as internal/external rotation which is the rotation in the transverse plane.

Adduction/abduction

The floating K_3 axis is perpendicular to K_1 axis and K_2 axis. We quantify the rotation angle around K_3 axis as adduction/abduction which is the rotation in the coronal plane.

Experiments

Both in vitro and in vivo experiments were conducted in a motion analysis laboratory with 16 infrared cameras with a sampling frequency of 100 Hz. An ultrasound (US) device (*LOGIQ 7, GE, USA*) was used to scan the target object at 23 Hz (45 mm US depth). We attached four markers on the (*ML 6-15*) US transducer as a local coordinate reference for the US probe. All the collected data were processed in MATLAB (MathWorks, R2014a, US) on a desktop computer (8-core Intel Core i7-4770 3.40 GHz running a 64-bit Windows OS).

In vitro experiment

To validate the accuracy of the CAT & MAUS system, an in vitro experiment on a ball-joint proximal femur phantom with detailed specification [22] was carried out. A ball joint was fixed in a sawbones femur head to mimic the hip socket joint so that the entire phantom could be rotated in three degrees of freedom (3DOF). We clamped the femur phantom in a water tank. The water tank had a plastic membrane window in the front surface through which the ultrasound wave can pass to scan the femur phantom, shown in Fig. 7. Degassed water was added to the water tank to submerge the greater trochanter (GT), which was our target bony structure, but not the markers attached to the femur phantom as the marker positions cannot be captured by the motion analysis system under water. The femur phantom was rotated and fixed at five different positions with one vertical position as a reference position.

The GT of the femur phantom was scanned approximately in parallel at five different positions. The bone structure in each frame was segmented using the automatic bone segmentation method described in "Motion analysis with ultrasound system" section. The segmented result was compared to the manually segmented ground truth from two experts in bone US. Each expert repeated the segmentation three times.

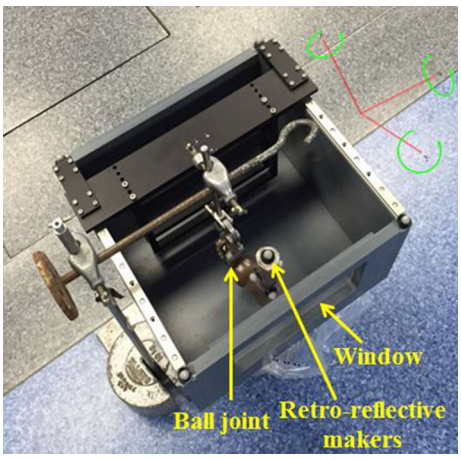

Fig. 7 In vitro experiment with a ball-joint proximal femur phantom clapped in a water tank

By referring to the positions of the US probe during the scan, a 3D surface of the GT was reconstructed from the segmentation of the bony structure in 2D US slices. The surfaces of the GT at four different positions were registered to the vertical reference position using GO-ICP in "Automatic bone segmentation" section. The four markers attached on the femur phantom were captured by the motion analysis system at those five different positions to provide the ground truth.

In vivo experiment

Ten healthy volunteers (5 males and 5 females) with a mean age of 26 years (range 18–36 years) were recruited. Anthropometric parameters were measured including the height, weight, left leg and foot lengths. Analysis was done on the left leg of each subject. All the volunteers were slim to average body-build weighted from 49 to 68 kg with heights from 160 to 185 cm. Calculated from their height and weight, the average body mass index (BMI) is 20.15 (range 18.9–21.7). The average left leg length of the females was 91.2 and 99.3 cm for males. Their average left foot length was 23.3 for females and 25.7 cm for males. Retro-reflective markers were attached on the lower limbs of a volunteer as illustrated in Fig. 6. Each volunteer was asked to perform typical gait poses, i.e. heel strike, mid stance, toe off and mid swing [23].

At each position, the left GT of the volunteer was located by palpation before US scanning was initiated. Then, the GT was scanned in an approximately parallel sweep using the 2D US device as in [15]. We scanned the GT by sweeping the US probe downwards along the long axis of the femur for approximately 15 cm. The size of all US images was 500 × 562 pixels (approx. 0.09 mm per pixel). We randomly selected 120 bone (greater trochanter) US images and segmented the bony structure in every 2D US slice and reconstructed surfaces for each position. A ground truth was constructed from a manual segmentation by two orthopaedic clinicians. The average intra-observer error over three segmentations on the same US image was 1.2 pixels, while the average inter-observer error over two observers was 1.4 pixels. Our automatic segmentation was compared with the ground truth, and the results using the method are described in [5] with their suggested parameters. The reconstructed surface of the GT at the four different positions were registered to the surface reconstructed at the standing position.

The GT at a standing position was registered to the four gait poses. Based on the hip joint kinematics descriptor in "Globally optimal 3D surface registration" section, we calculated the rotation angles of the hip joint rotation during gait which are presented in "In vivo experiment" section.

Results

Automatic bone segmentation

The probability maps obtained by employing our method and the method in [5] are shown in Fig. 8a, b, respectively, for visual comparison. The probability of the bone structure is significantly enhanced by employing local phase feature symmetry and integrated backscattering energy, i.e. our method reduces the number of false probability responses observed using method in [5].

Typical segmentation examples, two from the femur phantom (Fig. 9a, b) and two from the volunteers (Fig. 9c, d) with the manual segmentation (red line) and automatic segmentation with both our method (white line) and the method in [5] (blue line), are shown in Fig. 9.

There is no significant difference between our method and the method in [5] with their suggested parameters for the case of segmenting the femur phantom. However, incorrect detection of the soft tissues appeared in the in vivo data set using Foroughi et al.'s method [5] because in that method soft tissues with high intensity values produce high values in the

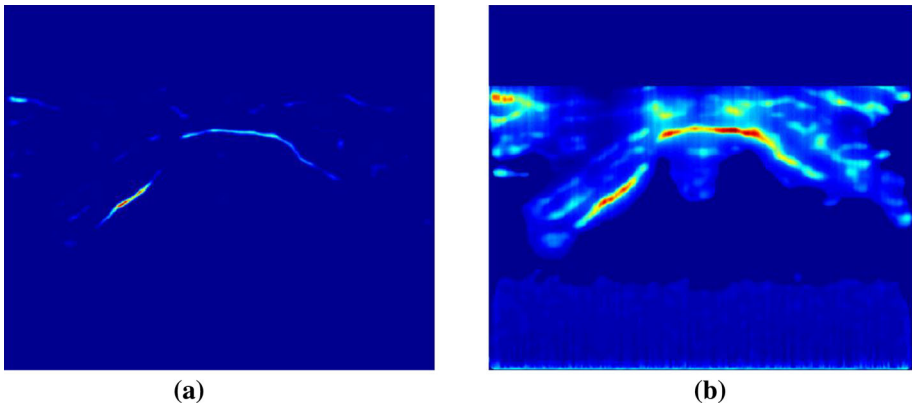

Fig. 8 Probability map comparison, **a** probability map of our method, **b** probability map of the method in [5]

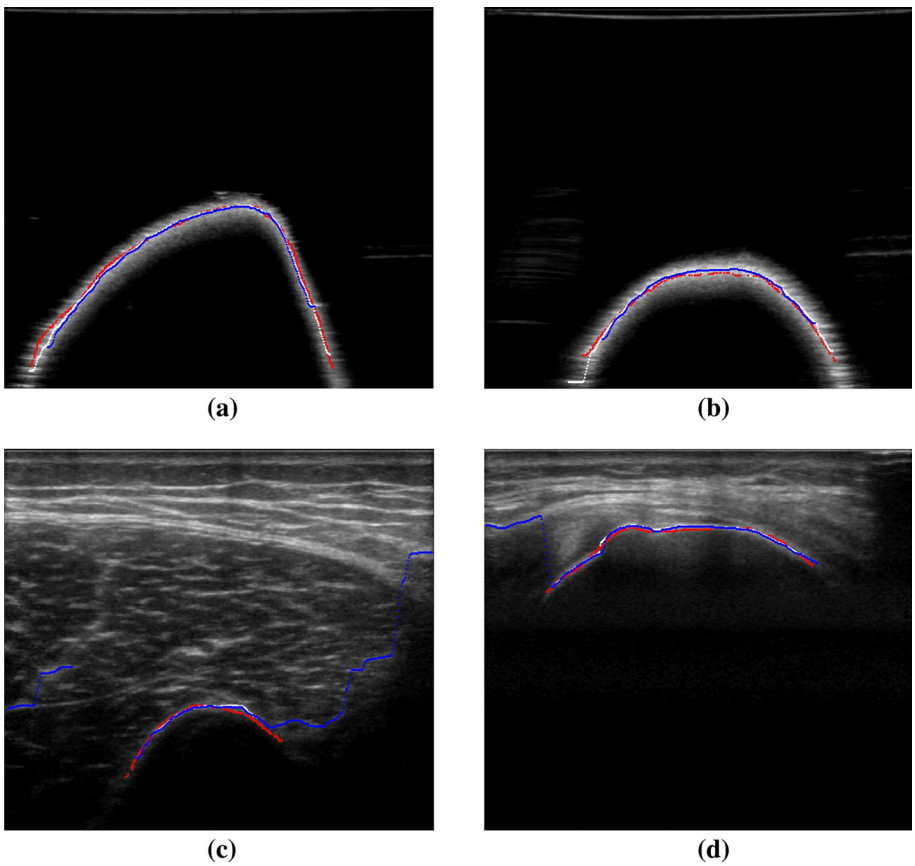

Fig. 9 Automatic segmentation with our method (*white line*),and with previous method in [5] (*blue line*), and the manually segmented ground truth (red line) for four typical segmentation examples of the greater trochanter. All the segmentation results are dilated for better visualization

Table 2 Error comparison of segmentation with different threshold values

Threshold	Erroneous detection (frame)	Missed detection (frame)	Max. ED error (pixel)	Average percentage (%)
Our method				
0.10	19	0	1.0718	62.46
0.12	10	0	1.2369	59.39
0.15	*2*	*0*	*1.3341*	*57.26*
0.18	1	5	1.3731	52.33
0.20	1	13	1.3775	50.36
Best result using the method in [5]				
0.55	2	6	1.3463	51.21 %

The threshold highlighted in italics gave best results

bone probability map. Since we used multi-scaled bandpass filters to enhance bone structure probability, we eliminated those unwanted soft tissue responses efficiently. As explained in "Motion analysis with ultrasound system" section, a threshold was not directly applied to US images but on the bone probability map. When the probability map was thresholded with a high value, the erroneous detections of the soft tissue were reduced; however, the bone structure might not be completely detected, and vice versa for a low threshold. A comparison between the ground truth (from manual segmentation), the results using our method with different thresholds, and the best result on the same data set using the method in [5] is shown in Table 2. In the comparison, the number of erroneous detection frames, where there are false positive detections, is counted and listed in the second column. The number of missed detection frames, where there is no true positive detection, is counted and listed in the third column. As the bone probability map gives a low response at the ends of the visible bone region, the automatic segmentation is never longer than the manual segmentation. Therefore, the maximum Euclidean distance (ED) error in pixels between the true positive automatic segmentation and the manual segmentation of the same length is listed in the fourth column. The average percentage of pixels on the ground truth path that are correctly segmented within the clinical tolerance ± 0.5 mm (approximately 5 pixels) is calculated over the whole data set and shown in the last column of Table 2.

In many cases, the spatial extent of the automatically segmented bone was less than that of the full manual segmentation, which leads to low overlapping percentages. This is because of the indistinct appearance at the edges of the bone structure. However, the detection of the full extent of the bone is not necessary for accurate registration later in the post-processing pipeline. Since the range of the probability maps with our method and the method in [5] is different, we compared our method with different threshold values to the manual segmented ground truth and the best result on the same data set using the method in [5]. When a lower threshold was applied on the probability map, there are more frames with erroneous detections and fewer frames with no detection, and vice versa. A threshold of 0.15 gave the best performance for our data set, which is highlighted in Table 2.

We counted the average execution time of a single US image segmentation over 120 US images with our method and Foroughi's method [5]. An US image with pixel size 500×562 was segmented in approximately 4.1 s while the algorithm in [5] took around 5.3 s as more pixels satisfied the threshold criteria in the latter case.

Globally optimal 3D surface registration

We tested the GO-ICP registration method with a synthetic GT surface point cloud rotated from 10° to 350° around the x, y and z axes. We ran the registration algorithms at every 10° change in position around each axis. The GO-ICP registration algorithm was compared with the traditional ICP algorithm without a good initialization shown in Fig. 10. Registration angle errors of GO-ICP and traditional ICP registration for seven selected rotation angles (10°, 50°, 120°, 180°, 240°, 310° and 350°) representing the full 360° rotations are listed in Table 3.

From Fig. 10 and Table 3, we can see that the traditional ICP failed at many angles without a good initialization, while GO-ICP performed well at any angle because of the global optimization search.

In our femur phantom experiments, the average rotation errors of X,Y,Z axes were 0.52°, 0.55° and 0.071° with the standard deviations of 0.90°, 1.15° and 1.13°, respectively over 3 trials of the proximal femur phantom shown in Fig. 11.

The elapsed time for one registration was approximately 20 s which is slower than the time elapsed for normal ICP (0.23 s) as extra time is required for the global optimization search.

In vivo experiment

The flexion/extension, adduction/abduction and internal/external rotation angles at the four gait positions are shown

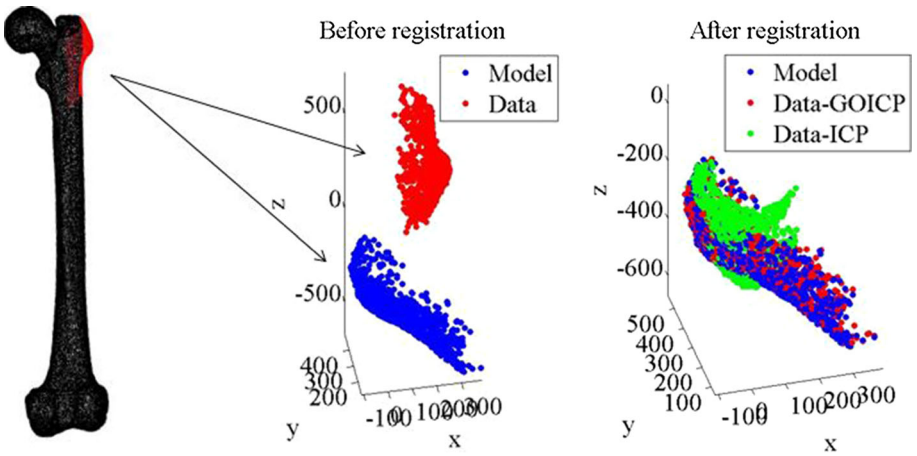

Fig. 10 A comparison between the globally optimal iterative closest point registration algorithm and the traditional iterative closest point registration algorithm on the GT surfaces reconstructed from US scans at two different positions

Table 3 Registration error comparison of relative rotation at different angles between globally optimal ICP and traditional ICP

Rotation angle (°)	Globally optimal ICP			Traditional ICP		
	X (°)	Y (°)	Z (°)	X (°)	Y (°)	Z (°)
10	0.26	−0.53	−2.59	0.18	−0.33	−0.87
50	−0.18	0.45	−2.38	−4.77	0.28	−6.04
120	0.15	0.32	3.64	−134.76	−164.23	−14.71
180	0.07	0.16	−1.58	142.42	−172.38	−15.10
240	0.22	0.21	2.32	−172.49	−60.48	14.42
310	0.32	0.11	2.05	−3.14	2.34	7.44
350	−0.28	0.28	1.64	−0.38	−0.95	2.63

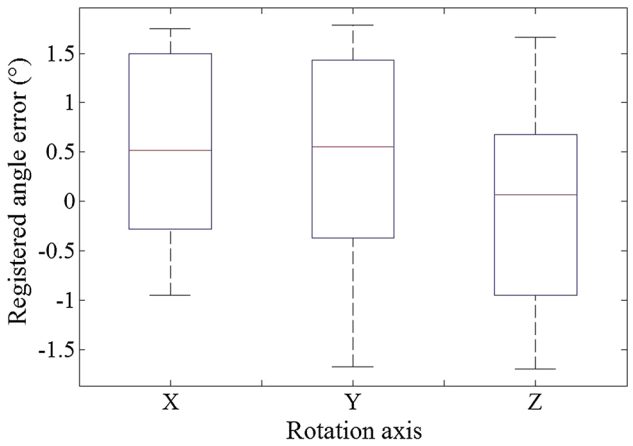

Fig. 11 Registered angle errors of the proximal femur phantom data around *X*, *Y* and *Z* axes compared to the ground truth caputed by the motion analysis system

in Fig. 12. Because of the different individual step stride, the flexion/extension angles vary from −14.34° to 33.22° with a standard deviation of 5.97°, the adduction/abduction angles vary from −2.73° to 1.02° with a standard deviation of 4.23° and the internal/external rotation angles vary from −0.05° to 3.38° with a standard deviation of 1.77°. As all the volunteers were healthy and without any hip joint injuries or operations, Fig. 12 provides a motion trend of hip joint rotations of a healthy subject during gait. Interestingly, the motion trend in Fig. 12 resembles the trend presented in [24]. Specifically, the hip joint rotations measured with the CAT & MAUS system are similar to the results modelled by a Euler model reported in [24] with a maximum error of 4° because of the different step stride.

Discussion

In our work, we have developed and validated a computer-aided post-processing pipeline to assist in a motion analysis with ultrasound (MAUS) system for describing joint kinematics. The post-processing pipeline consists of a bone segmentation algorithm and a globally optimal ICP registration algorithm, which makes the MAUS system more accurate and robust. In order to reconstruct a 3D surface of the bone, a quasi-static acquisition is required. However, the computer-aided tracking and motion analysis with ultrasound (CAT & MAUS) system was shown to significantly reduce the test time on one subject from 30–40 to 3–5 min. The CAT & MAUS system has been validated on a proximal femur phantom. The accuracy of the femur rotation was less than 1.2° which is a similar accuracy to that reported from the estimated model in [24].

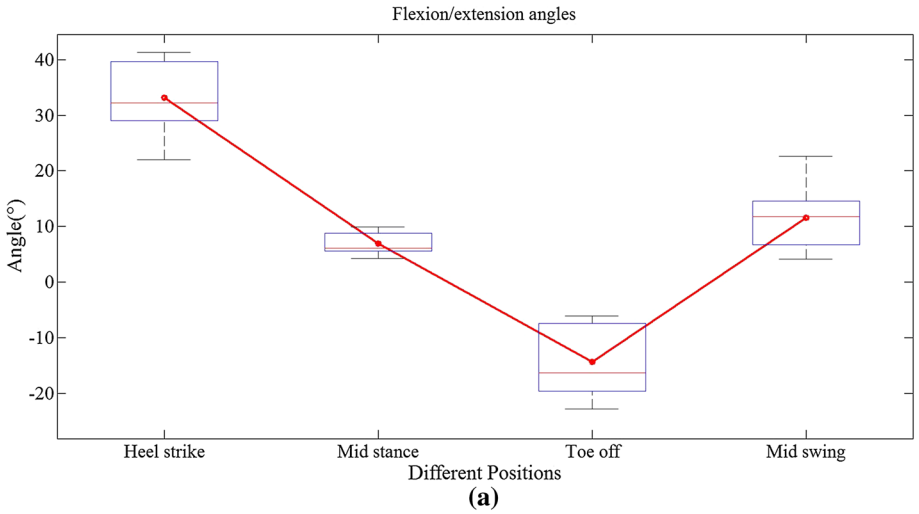

(a)

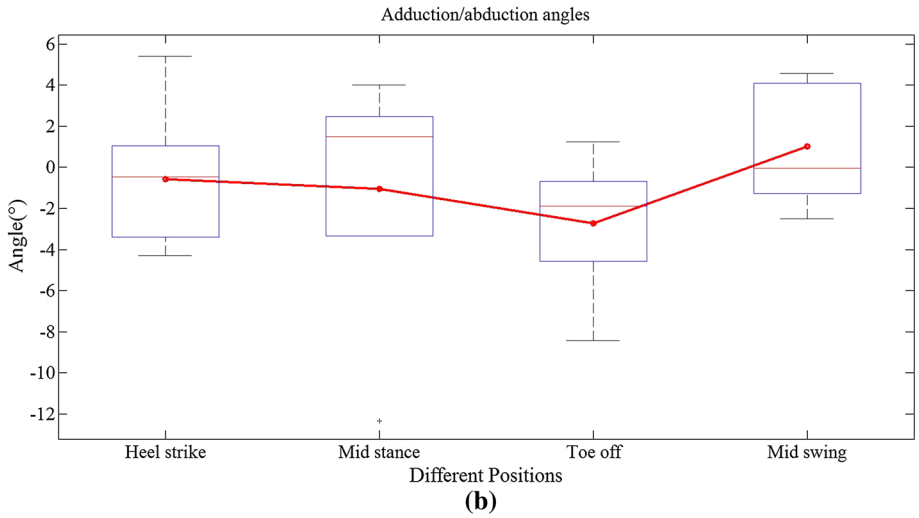

(b)

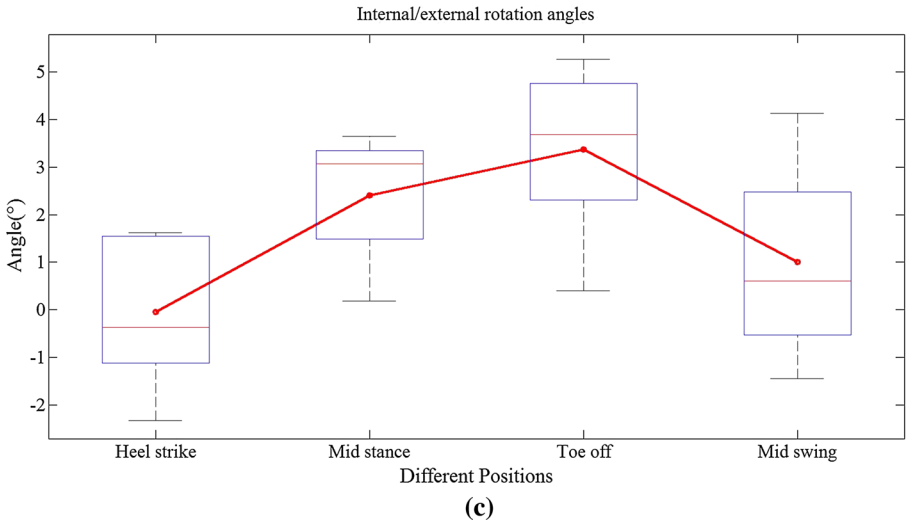

(c)

Fig. 12 Hip joint rotation angles, **a** flexion/extension, **b** adduction/abduction and **c** internal/external rotation

In our approach, subjects do not need to be CT scanned as required for instance with the method presented in [8]. In our study, a 3D surface of the greater trochanter was scanned and reconstructed using ultrasound instead of CT as the registration reference. Other joints could be scanned for different clinical research interests.

The results from the ten volunteers provided a generic hip joint kinematics model of healthy subjects. However, as the step strides of the subjects were different, the standard deviations of the hip joint rotations between subjects were up to 5°. An assistive device to constrain the movements could be considered to minimize the deviation between subjects caused by physical parameter differences, i.e. height, weight and so on. A standardized scanning protocol could be defined for the ease of real world clinical use.

Conclusion

In this paper, we have presented a computer-aided tracking and motion analysis with ultrasound system to describe hip joint kinematics. The measurements of the greater trochanter are acquired using the motion analysis with ultrasound system. Post-processing includes automatic bone detection and globally optimal ICP registration to quantify the joint rotation angles in 3DOF using an adapted International Society of Biomechanics's recommendation of joint kinematics description. Both the maximum absolute errors of segmentation ($\leqslant$0.2 mm) and registration ($<4°$) are within the clinical tolerance [19,25]. The in vivo trials demonstrated how the hip joint rotates in 3DOF and provided a motion trend of healthy subjects during gait. We have shown that the system can model hip joint kinematics of healthy subjects. In future work, we will investigate how our system can be used to distinguish clinically relevant joint conditions using the current data as a reference.

Acknowledgments The authors would like to thank Orthopaedics Research UK for supporting this project (Grant code: HFR00390) and the China Scholarship Council for funding Rui Jia (CSC NO.201408-060234). We sincerely thank all the participants for volunteering in the experiments.

Compliance with ethical standards

Conflict of interest The authors declare that they have no conflict of interest.

Ethical standard All the in vivo experiments were in accordance with the ethical standards of the institutional and/or national research committee.

References

1. Department of Health (2006) The musculoskeletal services framework—a joint responsibility: doing it differently. Technical report
2. Powers CM (2003) The influence of altered lower-extremity kinematics on patellofemoral joint dysfunction: a theoretical perspective. J orthop Sports Phys Ther 33(11):639–646. doi:10.2519/jospt.2003.33.11.639
3. Monk AP (2011) The patellofemoral joint: form and function, Ph.D. thesis, University of Oxford
4. Peters A, Galna B, Sangeux M, Morris M, Baker R (2010) Quantification of soft tissue artifact in lower limb human motion analysis: a systematic review. Gait Posture 31(1):1–8
5. Foroughi P, Boctor E, Swartz MJ, Taylor RH, Fichtinger G (2007) Ultrasound bone segmentation using dynamic programming, in: IEEE ultrasonics symposium proceedings, pp 2523–2526. doi:10.1109/ULTSYM.2007.635. http://ieeexplore.ieee.org/lpdocs/epic03/wrapper.htm?arnumber=4410208
6. Hacihaliloglu I, Abugharbieh R, Hodgson AJ, Rohling RN (2009) Bone surface localization in ultrasound using image phase-based features. Ultrasound Med Biol 35(9):1475–1487. doi:10.1016/j.ultrasmedbio.2009.04.015
7. Hacihaliloglu I, Abugharbieh R, Hodgson AJ, Rohling RN, Guy P (2012) Automatic bone localization and fracture detection from volumetric ultrasound images using 3-D local phase features. Ultrasound Med Biol 38(1):128–144. doi:10.1016/j.ultrasmedbio.2011.10.009
8. Wein W, Karamalis A, Baumgartner A, Navab N (2015) Automatic bone detection and soft tissue aware ultrasound-CT registration for computer-aided orthopedic surgery. Int J Comput Assist Radiol Surg 10(6):971–979. doi:10.1007/s11548-015-1208-z. http://link.springer.com/10.1007/s11548-015-1208-z
9. Kowal J, Amstutz C, Langlotz F, Talib H, Ballester MG (2007) Automated bone contour detection in ultrasound B-mode images for minimally invasive registration in computer-assisted surgery—an in vitro evaluation. Int J Med Robot Comput Assist Surg 3(4):341–348. doi:10.1002/rcs.160
10. Zhang Z (1994) Iterative point matching for registration of free-form curves and surfaces. Int J Comput Vis 13(2):119–152. doi:10.1007/BF01427149. http://link.springer.com/10.1007/BF01427149
11. Fitzgibbon AW (2003) Robust registration of 2D and 3D point sets. Image Vis Comput 21(13–14):1145–1153. doi:10.1016/j.imavis.2003.09.004. http://linkinghub.elsevier.com/retrieve/pii/S0262885603001835
12. Yang J, Li H, Jia Y (2013) Go-ICP: solving 3D registration efficiently and globally optimally. 2013 IEEE international conference on computer vision 1457–1464 doi:10.1109/ICCV.2013.184. http://ieeexplore.ieee.org/lpdocs/epic03/wrapper.htm?arnumber=6751291
13. Barratt DC, Penney GP, Chan CSK, Slomczykowski M, Carter TJ, Edwards PJ, Hawkes DJ (2006) Self-calibrating 3D-ultrasound-based bone registration for minimally invasive orthopedic surgery. IEEE Trans Med Imaging 25(3):312–323. doi:10.1109/TMI.2005.862736
14. Monk AP, Chen M, Mellon S, Gibbons M, Beard DJ, Murray DW, Gill HS (2013) Comparison of in vivo coronal plane patella tracking following knee arthroplasty using the MAUS technique. Bone Jt J Orthop Proc Suppl 95(SUPP 26):10
15. Jia R, Mellon S, Monk P, Murray D, Noble JA (2015) Three dimensional freehand ultrasound reconstruction using hybrid interpolation. In: Medical image understanding and analysis, Lincoln, UK, pp 169–174
16. Felsberg M, Sommer G (2001) The monogenic signal. IEEE Trans Signal Process 49(12):3136–3144. doi:10.1109/78.969520. http://ieeexplore.ieee.org/lpdocs/epic03/wrapper.htm?arnumber=969520
17. Rajpoot K, Grau V, Noble JA (2009) Local-phase based 3d boundary detection using monogenic signal and its application to real-time 3-d echocardiography images. In: Proceedings—2009 IEEE international symposium on biomedical imaging: from nano to macro, ISBI 2009, pp. 783–786. doi:10.1109/ISBI.2009.5193166
18. Kovesi P (1999) Symmetry and asymmetry from local phase. In: Tenth Australian joint conference on artificial intelligence, pp 190–196

19. Jia R, Hansjee S, Monk AP, Murray DW, Mellon SJ, Noble JA (2016) Automatic bone segmentation in ultrasound images using local phase features and dynamic programming. In: 2016 IEEE 13th international symposium on biomedical imaging (ISBI)
20. Jia R, Monk AP, Murray DW, Mellon SJ, Noble JA (2015) Greater trochanter tracking in ultrasound imaging during gait. In: 2015 IEEE 12th international symposium on biomedical imaging (ISBI), IEEE, pp 260–263
21. Wu G, Siegler S, Allard P, Kirtley C, Leardini A, Rosenbaum D, Whittle M, D'Lima DD, Cristofolini L, Witte H, Schmid O, Stokes I (2002) ISB recommendation on definitions of joint coordinate system of various joints for the reporting of human joint motion–part I: ankle, hip, and spine. International Society of Biomechanics. doi:10.1016/S0021-9290(01)00222-6
22. Sawbones, Biomechanical test materials (2014) www.sawbones.com
23. MTR, Gait assessment (2014) http://www.massagetherapyreference.com/gait-assessment/
24. Ramakrishnan H, Kadaba M (1991) On the estimation of joint kinematics during gait. J Biomech 24(10):969–977
25. Billuart F, Devun GOSWL, Mitton D (2007) 3D kinematics of the glenohumeral joint during abduction motion: an ex vivo study. Surg Radiol Anat 29(4):291–295. doi:10.1007/s00276-007-0208-2